City Research Online

City, University of London Institutional Repository

This is the published version of the paper.

This version of the publication may differ from the final published version.

research papers

Position-dependent shear-induced austenite–martensite transformation in double-notched TRIP and dual-phase steel samples

Romain Blondé,[a,b]* Enrique Jimenez-Melero,[c] Sathiskumar A. Ponnusami,[d] Lie Zhao,[b,e] Norbert Schell,[f] Ekkes Brück,[a] Sybrand van der Zwaag[g] and Niels van Dijk[a]

[a]Fundamental Aspects of Materials and Energy, Faculty of Applied Sciences, Delft University of Technology, Mekelweg 15, Delft, 2629 JB, The Netherlands, [b]Materials Innovation Institute, Mekelweg 2, Delft, 2628 CD, The Netherlands, [c]Dalton Cumbrian Facility, The University of Manchester, Westlakes Science and Technology Park, Moor Row, Cumbria CA24 3HA, UK, [d]Aerospace Structures and Computational Mechanics Group, Faculty of Aerospace Engineering, Delft University of Technology, Kluyverweg 1, Delft, 2629 HS, The Netherlands, [e]Department of Materials Science and Engineering, Delft University of Technology, Mekelweg 2, Delft, 2628 CD, The Netherlands, [f]Institute of Materials Research, Helmholtz-Zentrum Geesthacht, Max Planck Strasse 1, Geesthacht 21502, Germany, and [g]Novel Aerospace Materials Group, Delft University of Technology, Kluyverweg 1, Delft, 2629 HS, The Netherlands. Correspondence e-mail: r.j.p.blonde@tudelft.nl

While earlier studies on transformation-induced-plasticity (TRIP) steels focused on the determination of the austenite-to-martensite decomposition in uniform deformation or thermal fields, the current research focuses on the determination of the local retained austenite-to-martensite transformation behaviour in an inhomogeneous yet carefully controlled shear-loaded region of double-notched TRIP and dual-phase (DP) steel samples. A detailed powder analysis has been performed to simultaneously monitor the evolution of the phase fraction and the changes in average carbon concentration of metastable austenite together with the local strain components in the constituent phases as a function of the macroscopic stress and location with respect to the shear band. The metastable retained austenite shows a mechanically induced martensitic transformation in the localized shear zone, which is accompanied by an increase in average carbon concentration of the remaining austenite due to a preferred transformation of the austenite grains with the lowest carbon concentration. At the later deformation stages the geometry of the shear test samples results in the development of an additional tensile component. The experimental strain field within the probed sample area is in good agreement with finite element calculations. The strain development observed in the low-alloyed TRIP steel with metastable austenite is compared with that of steels with the same chemical composition containing either no austenite (a DP grade) or stable retained austenite (a TRIP grade produced at a long bainitic holding time). The transformation of metastable austenite under shear is a complex interplay between the local microstructure and the evolving strain fields.

1. Introduction

Low-alloyed transformation-induced-plasticity (TRIP) steels were developed in the late 1980s (Matsumura *et al.*, 1987*a*,*b*; Chen *et al.*, 1989) and have ever since attracted significant interest for automotive applications owing to their outstanding combination of high strength and formability (Srivastava *et al.*, 2006; Skálová *et al.*, 2006; Oliver *et al.*, 2007; Kammouni *et al.*, 2009; Chiang *et al.*, 2011). At room temperature a typical TRIP steel microstructure contains three phases: ferrite, bainite and metastable austenite (Timokhina *et al.*, 2004; Zaefferer *et al.*, 2004). The remarkable mechanical properties of this material are attributed to the combined effect of the multiphase microstructure and the transformation of the soft metastable austenite phase into the hard martensite phase upon activation by mechanical and/or thermal stimuli. This phenomenon, called the TRIP effect, increases the work-hardening rate during plastic deformation and delays necking (Dan *et al.*, 2007; Jacques *et al.*, 2007). Our understanding of the mechanical parameters controlling the austenite stability under complex loading conditions remains limited.

Table 1
Chemical composition of the studied samples in wt% with balance Fe.

C	Mn	Si	Al	P
0.218	1.539	0.267	1.75	0.018

Previous *in situ* studies have examined the austenite stability by applying a uniaxial tensile load at room temperature (Tomota *et al.*, 2004; Muránsky *et al.*, 2008; Cong *et al.*, 2009; Jia *et al.*, 2009; Asoo *et al.*, 2011), by cooling the material below room temperature (van Dijk *et al.*, 2005) and by tensile deformation at selected temperatures (Blondé *et al.*, 2012). These experimental results led to the development of advanced micromechanical models for the multiphase TRIP microstructure (Lani *et al.*, 2007; Tjahjanto *et al*, 2008; Choi *et al.*, 2008, 2009). So far, limited work has been done to investigate the structural behaviour of TRIP steels under shear loading (Jacques *et al.*, 2007) and more complicated mechanical testing conditions (Lacroix *et al.*, 2008) in detail. Understanding the mechanical response of the microstructure under shear deformation is an essential step to control the sheet-forming process in TRIP steels for automotive applications (De Cooman, 2004). An accurate prediction of this process requires a deeper insight into the mechanical response in terms of the austenite-to-martensite transformation, the load partitioning between the constituent phases and the texture evolution during shear loading.

In this study, we have undertaken a spatially resolved characterization of the austenite evolution in the deformed area during shear loading by performing *in situ* high-energy synchrotron X-ray diffraction (XRD) experiments. In order to determine the austenite transformation behaviour and the local strain partitioning as a function of the distance from the central shear length, a single low-alloyed steel composition with three different microstructures has been investigated: a dual-phase steel without austenite, a TRIP steel with stable (*i.e.* non-transforming) austenite and a TRIP steel with metastable austenite. The relation between the macroscopic stress and the orientation-dependent martensitic transformation has been determined by a Rietveld refinement of the high-energy XRD data. The corresponding texture evolution in the centre of the shear band was monitored by rotation of the sample and will be discussed in a separate paper.

2. Experimental methods and data analysis

2.1. Sample preparation

The chemical composition of the studied TRIP steel is shown in Table 1. Double-notched plate specimens (Czichos *et al.*, 2006) with a shear length of 1 mm and a thickness of 1 mm were machined along the hot-rolling direction of the starting sheet material. The slits were at 45° with respect to the loading direction and had a width of 0.2 mm. The loading axis of the samples was chosen parallel to the rolling direction (RD). Three different microstructures were generated by the applied heat treatment. To start, all samples were annealed in a salt

bath for 30 min at an intercritical temperature of 1143 K in order to obtain about equal fractions of austenite and ferrite. The first microstructure was obtained by a direct quench to room temperature, creating a dual-phase steel (DP) containing about equal amounts of ferrite (α) and martensite (α'). The other two samples were quenched in a second salt
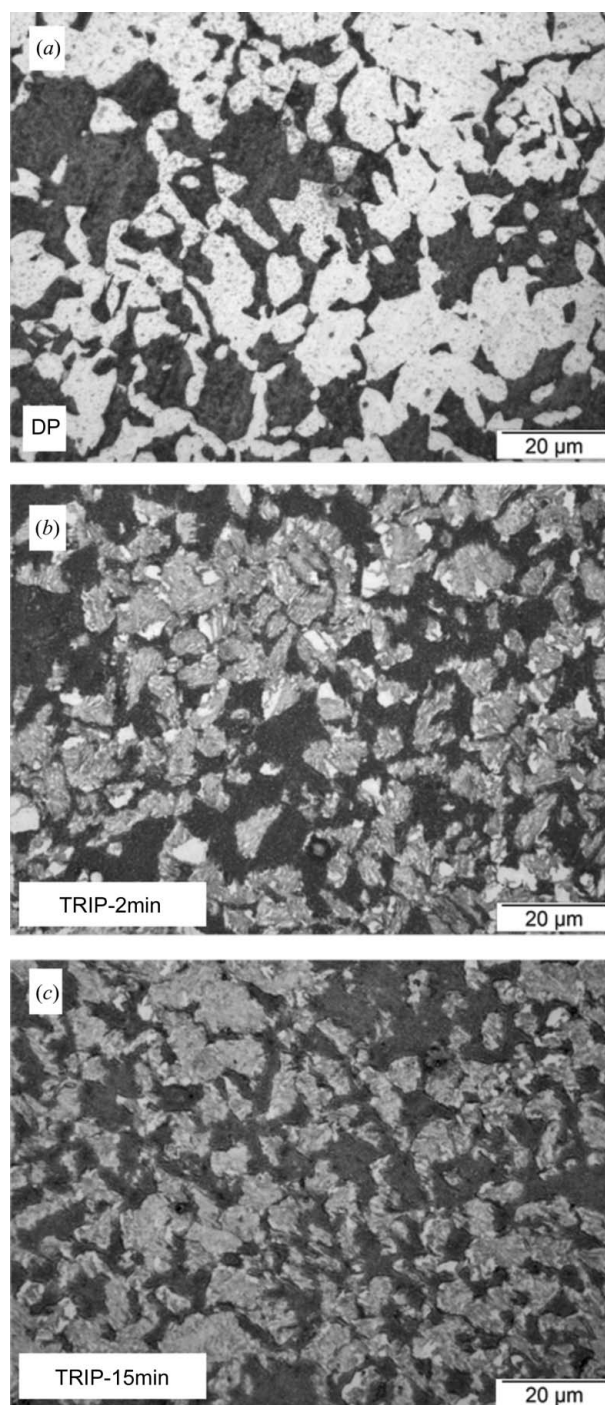
Figure 1
Initial microstructure of the studied samples: (*a*) DP, (*b*) TRIP-2min and (*c*) TRIP-15min. The DP microstructure contains a matrix of ferrite (black) and martensite (white). The TRIP microstructure contains a metastable austenite phase (white) within a matrix of ferrite (black) and bainite (grey) phases.

bath to a temperature of 673 K and held for either 2 min (TRIP-2min) or 15 min (TRIP-15min). During this isothermal holding the intercritical austenite transformed partly into bainite, resulting in a continuous enrichment of the interstitial carbon content in the untransformed austenite. The carbon-enriched austenite remained in a metastable state after a final water quench to room temperature. This heat treatment for the TRIP-2min and the TRIP-15min samples yielded a microstructure made of three constituents: ferrite (α), bainite (α_b) and metastable austenite (γ). In Fig. 1 the formed microstructures are shown.

2.2. *In situ* high-energy X-ray diffraction

The *in situ* XRD experiments were performed at the high-energy materials science beamline (P07) of the PETRA III synchrotron radiation source at DESY (Hamburg, Germany). Fig. 2 shows the sample geometry and the experimental setup used for the experiments. A monochromatic X-ray beam with an energy of 79.6 keV (wavelength of 0.156 Å) and a beam size of 100 × 100 µm illuminated the plate sample. For the high-energy X rays the sample absorption is relatively small, making it possible to study even 1 mm-thick samples in transmission geometry. The diffracted beam was recorded on a two-dimensional digital flat-panel X-ray detector (Perkin Elmer XRD 1622) placed 1025.1 mm behind the sample.

To study the mechanical response of the constituent phases, the sample was mounted on a 2 kN micro tensile tester placed on a translation table that provided alignment of the sample in three directions with respect to the X-ray beam. During the experiment, the samples were translated along (z axis) and transverse to (y axis) the loading axis in steps of 100 µm. We covered a rectangular area of 2.1 × 1.3 mm centred on the middle of the shear path (21 steps along y and 13 steps along z). The sample area monitored by the *in situ* microbeam X-ray diffraction experiments is indicated in red in Fig. 2. For each deformation step the strain was held constant during a complete set of diffraction measurements over the scanned sample area. During each translation step a two-dimensional diffraction pattern was recorded using an exposure time of 0.5 s. The instrument parameters for the X-ray diffraction setup were determined using a CeO$_2$ calibrant (NIST SRM 674b).

2.3. Analysis of diffraction data

The data measured consist of a series of 273 individual two-dimensional diffraction patterns covering the sample area of interest in (y, z) sample coordinates for each macroscopic deformation step. An integration over the azimuthal angles at constant scattering angle was performed using the *FIT2D* software package (Hammersley

et al., 1996) to obtain the corresponding one-dimensional diffraction patterns. A Rietveld refinement of the resulting one-dimensional X-ray diffraction patterns was performed using the *FullProf* package (Rodríguez-Carvajal, 1993) in order to determine the phase fraction and lattice parameter of the constituent phases as a function of the macroscopic strain. Fig. 3 shows examples of the two-dimensional X-ray diffraction patterns before and after applying a shear load, with the corresponding one-dimensional patterns analysed by the Rietveld method. Shear deformation leads to a reduction in peak intensity for the metastable austenite phase having a face-centred cubic (f.c.c.) structure and an increase in the diffraction peaks for the ferritic matrix having a body-centred cubic (b.c.c.) structure.

2.4. Finite element modelling

In order to study the relation between the (macroscopic) tensile load applied at the grips of the specimen and the local shear deformation induced in the central section owing to the slits, a two-dimensional finite element analysis was performed under plane stress conditions. The material behaviour is modelled using a classical J_2–Von Mises elasto-plastic constitutive law with isotropic hardening. The model parameters are calibrated from the uniaxial stress–strain response of the same material at 293 K as reported by Blondé *et al.* (2012). Consequently, the material model describes the effective behaviour of a large number of grains of all microstructural phases (austenite, ferrite, martensite). The inelastic deformation mechanisms occurring at individual phases (*e.g.* plastic deformation in the ferrite or phase transformation in retained austenite) are accounted for collectively as an effective inelastic deformation. Although the model is not intended for providing grain-scale information, it is suitable at the length scale of the specimen.
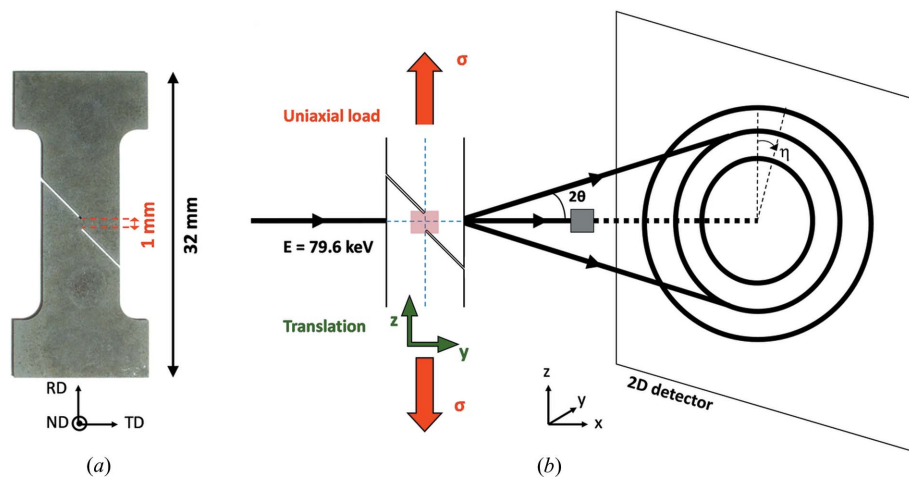
Figure 2
(*a*) Photograph of the shear specimen and (*b*) the experimental setup used for the high-energy microbeam X-ray diffraction experiments. The sample area of 2.1 × 1.3 mm scanned in steps of 100 µm is represented by a red rectangle at the crossing of the dashed lines.

3. Results and discussion

3.1. Macroscopic mechanical behaviour

Fig. 4 shows the mechanical response of the three steels deformed under shear load with a strain rate of $5.5 \times 10^{-4}\,\mathrm{s}^{-1}$. The relative displacement corresponds to the displacement of the grips normalized to the length of the shear section (1 mm) in the sample. Table 2 contains the relevant parameters that characterize the mechanical behaviour of the three samples. The difference in microstructure, resulting from the variation in bainitic holding time, results in a significant change in the mechanical response. Each sample was deformed step-wise in order to perform the X-ray diffraction experiments at constant macroscopic strain. Owing to the presence of about 50% of the hard martensite phase in the dual-phase steel, the

Table 2
Characteristic values for the macroscopic mechanical response of the steels deformed continuously under shear load for DP, TRIP-2min and TRIP-15min steels.

Steel notation	Bainitic holding time (min)	Yield strength (MPa)	Ultimate shear strength (MPa)	Elongation at yield strength (%)	Elongation at fracture (%)
DP	0	527	630	17.1	24.4
TRIP-2min	2	324	543	10.9	54.1
TRIP-15min	15	290	495	10.1	60.4

macroscopic stress–strain curve remains linear nearly up to fracture. The two TRIP microstructures also show a different response: the TRIP-2min sample shows a higher ultimate shear stress and a lower elongation at fracture compared to TRIP-15min. This difference is explained by the difference in
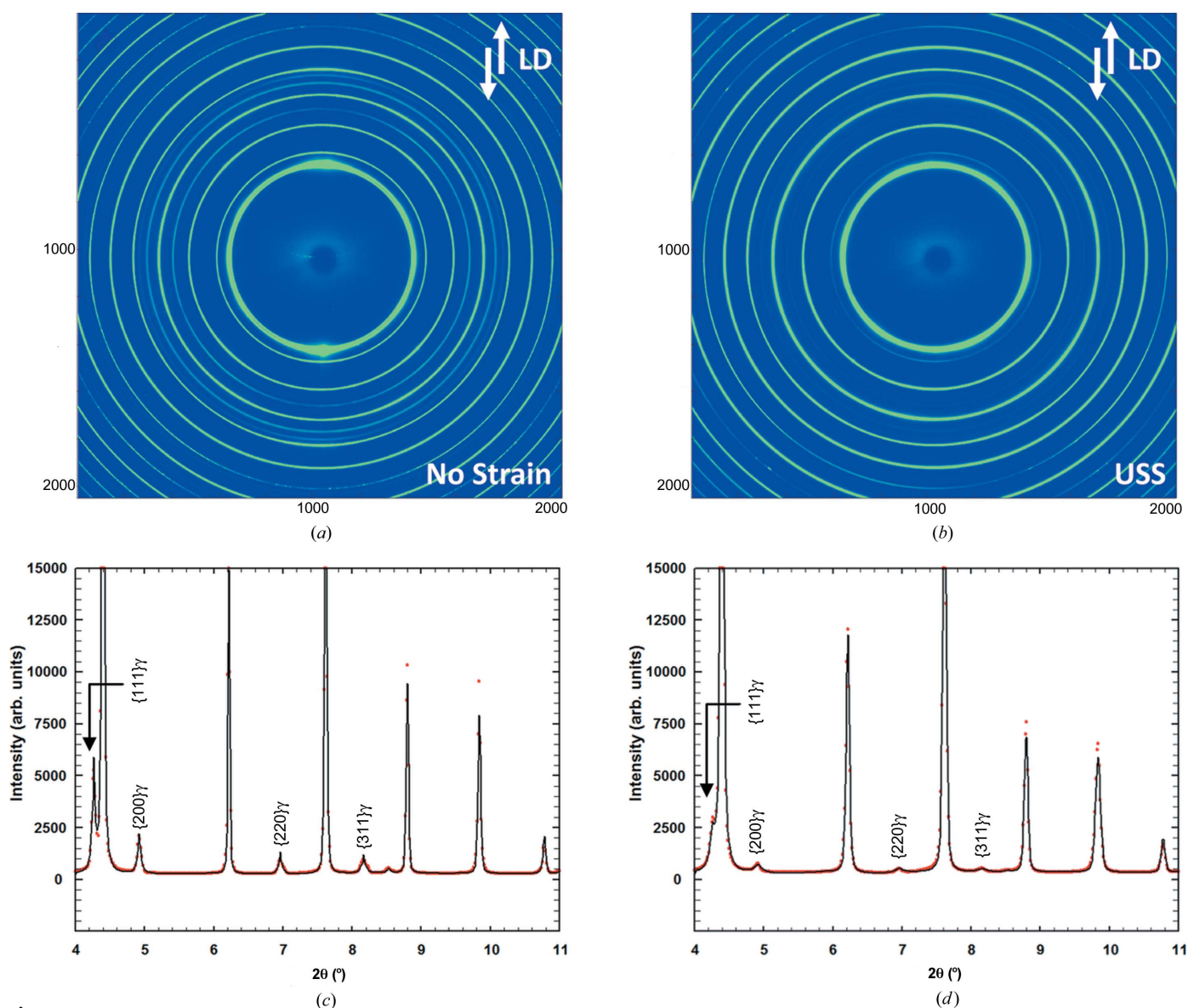
Figure 3
Two-dimensional X-ray diffraction patterns at (a) no strain and (b) ultimate shear strength (USS). The loading direction (LD) is indicated in the figure. The two-dimensional patterns were integrated over the azimuthal angles to obtain the one-dimensional X-ray patterns as a function of the scattering angle at (c) no strain and (d) ultimate shear strength. The corresponding Rietveld refinement of the one-dimensional X-ray patterns is also shown. The studied $\{111\}_\gamma$, $\{200\}_\gamma$, $\{220\}_\gamma$ and $\{311\}_\gamma$ austenite reflections have been labelled on the one-dimensional patterns.
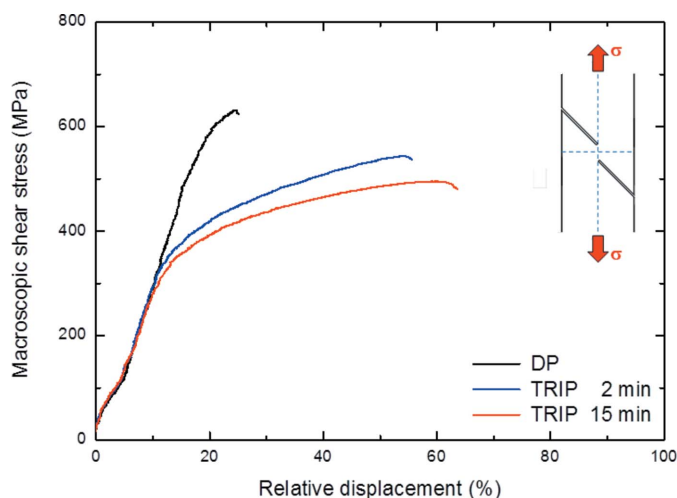
Figure 4
Macroscopic shear stress as a function of the relative displacement of the DP, TRIP-2min and TRIP-15min steels during shear loading.

fraction and average carbon content of the retained austenite phase present. The strong sensitivity of the macroscopic mechanical response to the microstructural parameters highlights the need to understand the microstructural evolution in TRIP steels in order to control and predict their mechanical properties.

3.2. Development of elastic shear strains

The elastic strain tensor can be determined by measuring the normal strains in various directions in the sample coordinates (1, 2, 3) = (RD, TD, −ND) (Noyan & Cohen, 1987), where RD is the rolling direction, ND the normal direction and TD the transverse direction of the plate sample. Note that RD is along the vertical loading axis and ND along the X-ray beam in the laboratory coordinate system. For this high-

energy X-ray diffraction experiment in transmission geometry, the orientation-dependent normal lattice strain $\varepsilon(\eta)$ can be described as (He, 2009)

$$\varepsilon(\eta) = \frac{a(\eta) - a_0}{a_0}$$
$$\simeq \left(\frac{\varepsilon_{11} + \varepsilon_{22}}{2}\right) + \left(\frac{\varepsilon_{11} - \varepsilon_{22}}{2}\right)\cos 2\eta + \varepsilon_{12}\sin 2\eta, \quad (1)$$

where η is the azimuthal angle on the two-dimensional detector placed behind the sample, a_0 is the lattice parameter at zero deformation and $a(\eta)$ is that in the deformed state. ε_{11}, ε_{22} and ε_{12} are the components of the strain tensor ε_{ij} in the sample coordinates. During deformation, the load is distributed between the austenite and the ferritic matrix. It is important to note that the relative change in the austenite lattice parameter can originate both from elastic strains and from a change in average carbon concentration. This change in average carbon content originates from the fact that retained austenite grains with a low carbon concentration preferentially transform earliest as they have a lower stability. In this case we find

$$\varepsilon(\eta) \simeq \left(\frac{\varepsilon_{11} + \varepsilon_{22}}{2}\right) + \left(\frac{\varepsilon_{11} - \varepsilon_{22}}{2}\right)\cos 2\eta + \varepsilon_{12}\sin 2\eta + \varepsilon_{C},$$
$$(2)$$

where ε_{C} is the relative change in lattice parameter caused by a change in average carbon content.

For the TRIP-2 min grade the average carbon concentration in the retained austenite is lower than that in the TRIP-15 min grade and hence a stronger evolution in average carbon content is expected.

The elastic shear strain component for both phases can be estimated by $\varepsilon_{12} = [\varepsilon(45°) − \varepsilon(−45°)]/2$, where $\varepsilon(45°)$ and $\varepsilon(−45°)$ are the relative changes in lattice parameter for an azimuthal angle of $\eta = 45°$ and $\eta = −45°$, respectively.

Fig. 5 shows the spatial distribution of the local shear strain ε_{12} in the area of interest at the initial undeformed state and at ultimate shear strength (USS) for the three samples. The particular design of the sample shows a clear development of a shear strain localized along the shear length. Note that the notches are observed at the bottom right and top left of the shear strain maps. For increasing load the shear band is found to rotate by about 5–10° with respect to the loading axis.

Fig. 6 shows the spatial profiles of the local shear strain for the ferritic matrix and the austenite phase in the DP, TRIP-2min and TRIP-15min samples for an increasing macroscopic shear load. The curves were obtained by an integration along the loading direction covering a length of 0.5 mm around the centre on the shear length. The profile of the shear band can roughly be described by a
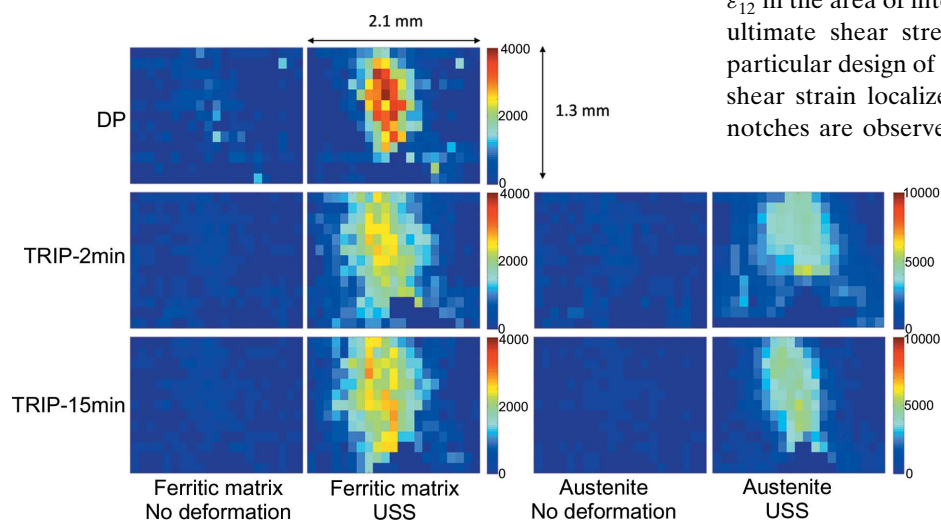
Figure 5
Spatial maps of the elastic shear strain ε_{12} (10^{-6}) in the ferritic matrix and the austenite at no deformation and at USS for the DP, TRIP-2min and TRIP-15min samples.

Gaussian function. For increasing shear load the shape of the profile is largely unchanged, while the maximum strain value increases linearly with the load until the yield point. Above this point a plastic deformation mode is activated, where the grains are yielding, and deviations from this linear behaviour are found. For the local shear strains these deviations are small. At USS, the ferritic matrix presents a shear band of about 2 mm for the TRIP microstructures and about 1 mm for the DP microstructure. The corresponding maximum shear strain in the ferritic matrix is $\varepsilon_{12}^{\alpha} \simeq 0.34\%$ for the DP micro-

structure and $\varepsilon_{12}^{\alpha} \simeq 0.25\%$ for the TRIP microstructures at USS.

Comparing the strain profile of the shear band in the ferritic matrix at fixed stress levels between 300 and 500 MPa, a higher maximum strain is observed at the centre of the shear band for the DP microstructure than for the two TRIP microstructures. This difference can be explained as resulting from the strain partitioning with the retained austenite phase in the TRIP steels. The retained austenite in the TRIP steels is only present in a relatively low volume fraction (<10%) but shows a significantly higher shear strain than the ferritic matrix.

The width of the shear band in the ferritic matrix is significantly higher for the two TRIP microstructures than for the DP microstructure for stress levels beyond 300 MPa. As the increase in width for the TRIP samples is most pronounced beyond the yield stress, it is expected to originate from the plastic deformation, which is negligible for the DP microstructure. The width of the shear band is comparable for both TRIP samples, which indicates that their elastic properties are similar.

In the TRIP-15min microstructure, the shear band shows a similar strain profile for both the austenite phase and the
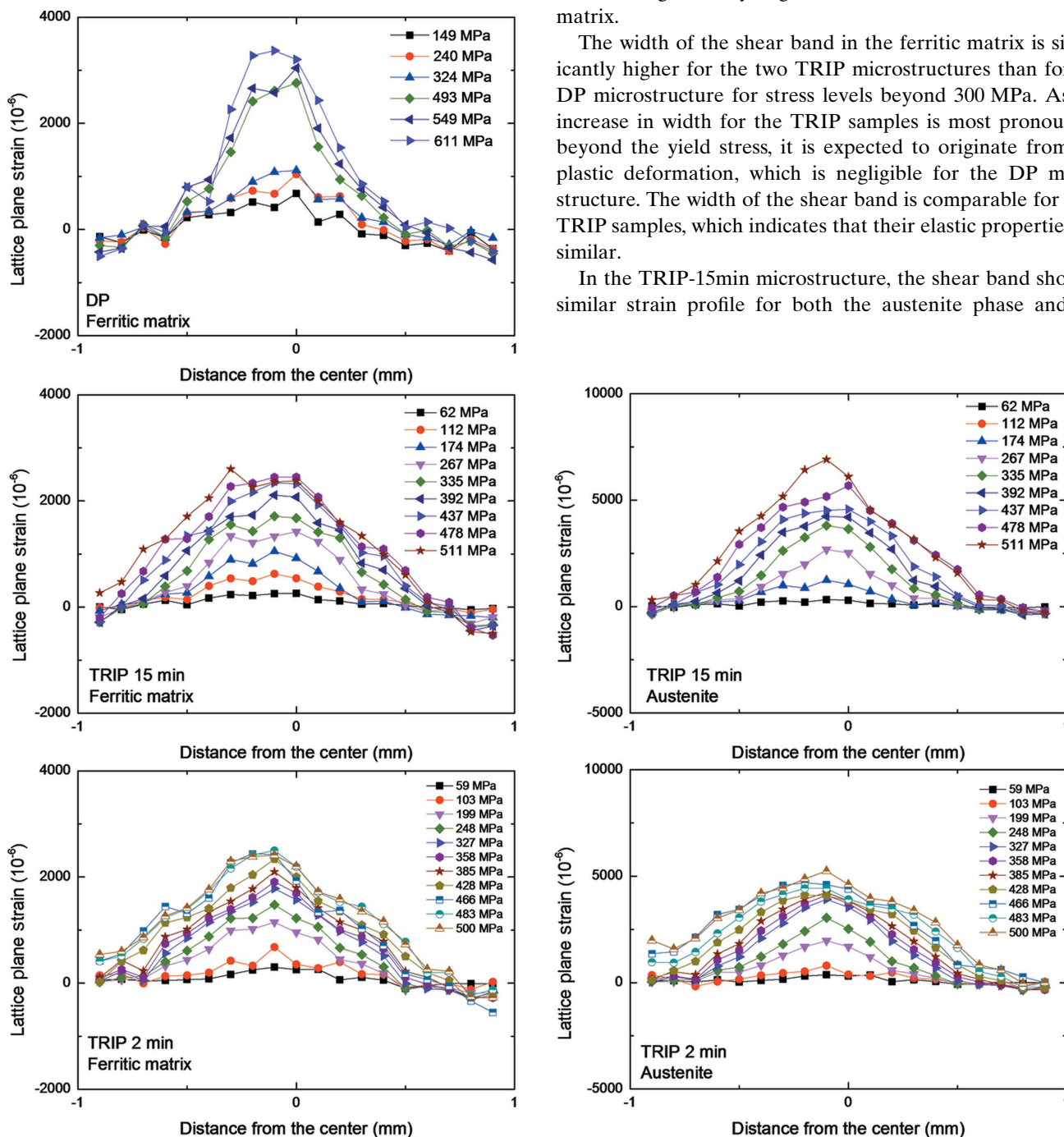
Figure 6
Elastic shear strain ε_{12} (10^{-6}) as a function of the distance from the middle of the shear band in the ferritic matrix and the austenite for the DP, TRIP-2min and TRIP-15min samples for the studied stress states.

ferritic matrix, as this microstructure is relatively stable during shear deformation. For the TRIP-2min sample, with a metastable austenite phase, the strain profile appears to flatten for austenite at the centre of the shear band and peak for the ferritic matrix. This may be caused by a local transformation of the relatively unstable austenite into martensite in the centre of the shear band.

3.3. Transformation behaviour of metastable austenite

The TRIP-2min sample, containing retained austenite with an optimal metastability for transformation under elastic–plastic deformation at room temperature, will be studied in more detail. Fig. 7 shows the elastic tensile strain ε_{11} and the elastic shear strain ε_{12} for the ferritic matrix and austenite, the austenite fraction, and the change in carbon concentration in the austenite for three stress states in the TRIP-2min sample. The maximum load of 327 MPa corresponds approximately to the yield point. For austenite, the tensile strain ε_{11} can be obtained by

$$\varepsilon_{11} = \frac{\varepsilon(0°) - \varepsilon(90°)}{1 + \nu}, \tag{3}$$

where $\nu = 0.367$ is the Poisson ratio of austenite (Blondé et al., 2012). The corresponding compressive strain amounts to $\varepsilon_{22} = -\nu\varepsilon_{11}$. The change in lattice parameter due to the evolution in average carbon content ε_C can now be estimated by

$$\varepsilon_C = \frac{\varepsilon(45°) + \varepsilon(-45°)}{2} - \left(\frac{1 - \nu}{1 + \nu}\right)\frac{\varepsilon(0°) - \varepsilon(90°)}{2}. \tag{4}$$

In the centre of the shear band only the first term significantly contributes up to the yield point. The experimental value of ε_C can directly be used to estimate the change in carbon concentration as the austenite lattice parameter is related to

chemical composition via the following relationship (van Dijk et al, 2005):

$$a_\gamma = 3.556 + 0.0453x_C + 0.00095x_{Mn} + 0.0056x_{Al}, \tag{5}$$

where a_γ is in Å and x_C, x_{Mn} and x_{Al} are in wt%.

For the TRIP-2min sample the initial austenite phase has a carbon content of $x_C = 1.30$ (2) wt%. Fig. 7 confirms that for the TRIP-2 min sample a shear band develops with increasing macroscopic shear load. In addition, we find that near the end of the notches an additional tensile component is generated for our sample geometry. These strain components can now be correlated to the decay of the austenite phase fraction and the increase in carbon concentration in the remaining austenite. It is found that in the middle of the shear band indeed the austenite phase fraction is strongly reduced, while the carbon concentration increases significantly. The transformation of metastable austenite is, however, not exclusively found in the shear band but also extends to the regions with a high tensile strain close to the end of the notches. This confirms that the transformation can be induced both by shear and by tensile deformation, as was already shown in dedicated experiments for transformation under uniform tensile stress (Blondé et al., 2012).

In Fig. 8 the spatial profiles of the local austenite shear strain, austenite fraction and change in average carbon concentration are shown for the TRIP-2min sample for increasing macroscopic shear load. The curves were obtained by an integration along the loading direction covering a length of 0.5 mm around the centre of the shear length. The local strain increases until fracture, while the austenite fraction continuously decreases, leading to a local increase in average carbon concentration. The carbon increase seems to saturate at a maximum value of $\Delta x_C \simeq 0.15$ wt%. The high degree of shear localization in the centre of the sample leads to a change in austenite volume fraction from about 8% prior to loading to a final volume fraction of about 3% at USS.
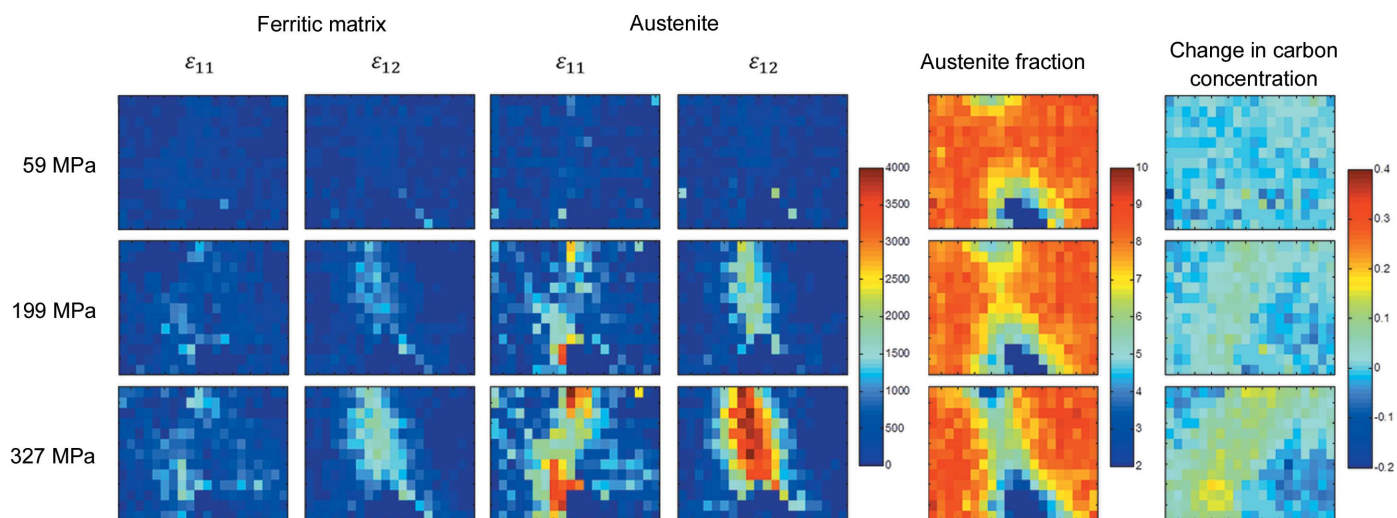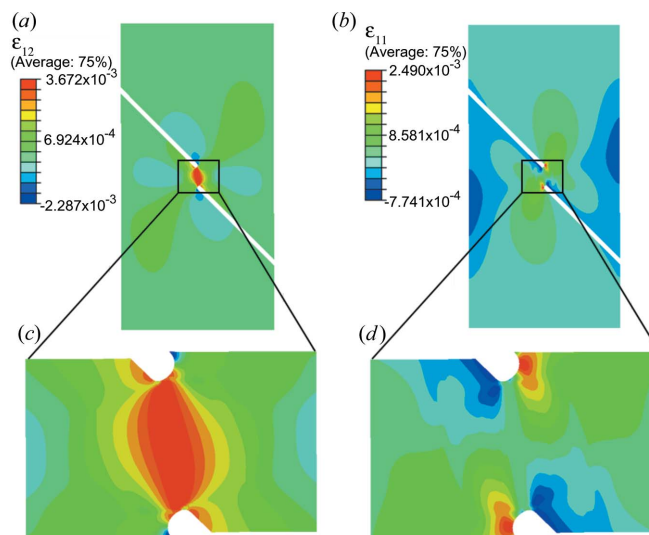

Figure 7
Spatial maps of the elastic shear strain ε_{12} (10^{-6}) and tensile strain ε_{11} (10^{-6}) for the ferritic matrix and the metastable austenite in the TRIP-2min sample at a macroscopic shear stress of 59, 199 and 327 MPa. The corresponding spatial maps of the austenite phase fraction f_γ (%) and the change in average carbon concentration in the austenite phase Δx_C (wt%) are also shown.
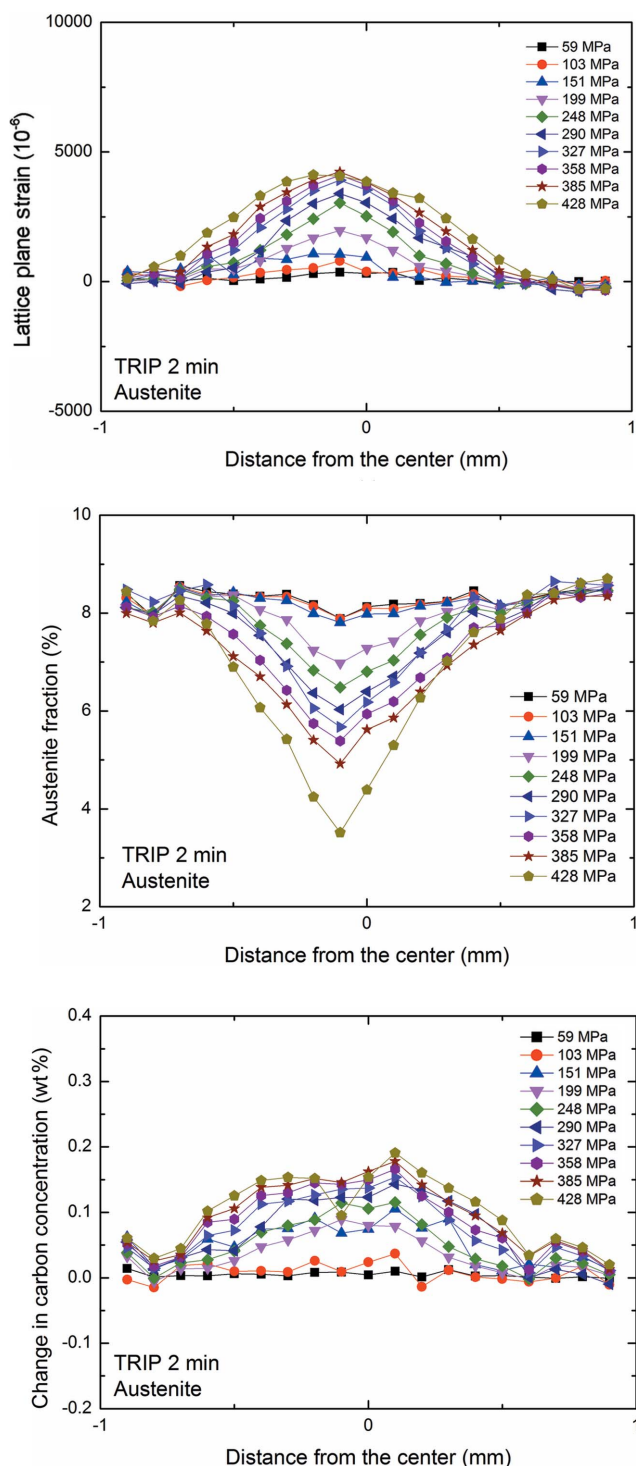
Figure 8
Elastic shear strain ε_{12}, phase fraction and change in average carbon concentration of the austenite phase in the TRIP-2min sample as a function of the distance from the middle of the shear band for the stress state studied.

Figure 9
Finite element method results for the shear sample geometry at yield strength. The local shear ε_{12} (a) and tensile ε_{11} (b) strains are represented over the full domain. The area measured by X-ray diffraction is shown in detail for ε_{12} (c) and ε_{11} (d).

3.4. Comparison with finite element modelling

Contour plots of the elastic strain components obtained from the finite element simulation at the macroscopic yield strength are shown in Fig. 9. The experimentally measured strain contours compare qualitatively well to the numerical predictions. As expected, the extension of the specimen at the grips is localized mostly as a shear deformation in a band-like region connecting the ends of the slits in the specimen [see ε_{12} component in Figs. 9(a) and 9(c)]. A similar strain state is indeed observed in the experimental data of Fig. 7. Outside of this banded region, the deformation is significantly smaller. Strains normal to the shear band [i.e. ε_{11} component shown in Figs. 9(b) and 9(d)] are concentrated near the ends of the slits but rapidly decay outside this region. These peak tensile regions can be purely attributed to the geometry of the shear specimen. The above arguments support that the observed phase transformation in fact takes place primarily in the regions under shear deformation. From the simulations, it is observed that the normal stress along the shear band is relatively small compared to the shear stress, implying that the applied load is predominantly felt as shear force by the midsection. This justifies the approximation of computing the average shear stress (mentioned as macroscopic shear stress in the above sections) as the total force at the grips divided by the nominal cross section of 1 mm^2 in the middle of the specimen.

4. Conclusions

We have performed in situ high-energy X-ray diffraction experiments at a synchrotron source in order to correlate the austenite transformation behaviour in TRIP steels to the local strain development during shear deformation. The main conclusions are as follows:

(1) The use of a microbeam of high-energy X-rays to scan the shear length of a double-notched specimen has proven to be a powerful method to monitor the austenite evolution under shear conditions, simultaneously with the occurrence of

Romain Blondé et al. · Austenite–martensite transformation in TRIP and DP steel **963**

shear and tensile components at different sample positions relative to the shear band.

(2) The maximum local shear stress and the width of the Gaussian shear band are dependent on the elastic properties of the material. The DP microstructure presents the narrowest strained zone, while both the TRIP microstructures present a similar behaviour.

(3) The evolution of the strain profile has been successfully simulated by finite element modelling under plane stress conditions using the classical Von Mises model. The simulations confirm the presence of strong shear strains in the centre of the shear length and the occurrence of additional tensile strains confined to the edge region of the notches.

(4) The austenite fraction evolution in the TRIP-2min sample is correlated to the degree of local shear strain. The continuous austenite transformation leads to an increase in the average carbon content. The local carbon content is found to play an important role in the austenite stability under shear deformation.

References

Asoo, K., Tomota, Y., Harjo, S. & Okitsu, Y. (2011). *ISIJ Int.* **51**, 145–150.

Blondé, R., Jimenez-Melero, E., Zhao, L., Wright, J., Brück, E., van der Zwaag, S. & van Dijk, N. (2012). *Acta Mater.* **60**, 565–577.

Chen, H. C., Era, H. & Shimizu, M. (1989). *Metall. Trans. A*, **20**, 437–445.

Chiang, J., Lawrence, B., Boyd, J. & Pilkey, A. (2011). *Mater. Sci. Eng. A*, **528**, 4516–4521.

Choi, K. S., Liu, W. N., Khaleel, M. A., Ren, Y. & Wang, Y. D. (2008). *Metall. Mater. Trans. A*, **39**, 3089–3096.

Choi, K., Liu, W., Sun, X. & Khaleel, M. (2009). *Acta Mater.* **57**, 2592–2604.

Cong, Z. H., Jia, N., Sun, X., Ren, Y., Almer, J. & Wang, Y. D. (2009). *Metall. Trans. A*, **40**, 1383–1387.

Czichos, H., Saito, T. & Smith, L. (2006). *Springer Handbook of Materials Measurement Methods.* Leipzig: Springer.

Dan, W., Zhang, W., Li, S. & Lin, Z. (2007). *Comput. Mater. Sci.* **40**, 101–107.

De Cooman, B. (2004). *Curr. Opin. Solid State Mater. Sci.* **8**, 285–303.

Dijk, N. van, Butt, A., Zhao, L., Sietsma, J., Offerman, S., Wright, J. & Vanderzwaag, S. (2005). *Acta Mater.* **53**, 5439–5447.

Hammersley, A. P., Svensson, S. O., Hanfland, M., Fitch, A. N. & Hausermann, D. (1996). *High Pressure Res.* **14**, 235–248.

He, B. B. (2009). *Two-Dimensional X-ray Diffraction.* Hoboken: Wiley and Sons.

Jacques, P., Furnémont, Q., Lani, F., Pardoen, T. & Delannay, F. (2007). *Acta Mater.* **55**, 3681–3693.

Jia, N., Cong, Z. H., Sun, X., Cheng, S., Nie, Z. H., Ren, Y., Liaw, P. K. & Wang, Y. D. (2009). *Acta Mater.* **57**, 3965–3977.

Kammouni, A., Saikaly, W., Dumont, M., Marteau, C., Bano, X. & Charaï, A. (2009). *Mater. Sci. Eng. A*, **518**, 89–96.

Lacroix, G., Pardoen, T. & Jacques, P. (2008). *Acta Mater.* **56**, 3900–3913.

Lani, F., Furnémont, Q., Van Rompaey, T., Delannay, F., Jacques, P. & Pardoen, T. (2007). *Acta Mater.* **55**, 3695–3705.

Matsumura, O., Sakuma, Y. & Takechi, H. (1987*a*). *Trans. ISIJ*, **27**, 570–579.

Matsumura, O., Sakuma, Y. & Takechi, H. (1987*b*). *Scr. Mater.* **21**, 1301–1306.

Muránsky, O., Šittner, P., Zrnik, J. & Oliver, E. C. (2008). *Metall. Mater. Trans. A*, **39**, 3097–3104.

Noyan, I. C. & Cohen, J. B. (1987). *Residual Stress: Measurement by Diffraction and Interpretation.* New York: Springer-Verlag.

Oliver, S., Jones, T. B. & Fourlaris, G. (2007). *Mater. Sci. Technol.* **23**, 55–62.

Rodríguez-Carvajal, J. (1993). *Physica B*, **192**, 55–69.

Skálová, L., Divišová, R. & Jandová, D. (2006). *J. Mater. Process. Technol.* **175**, 387–392.

Srivastava, A. K., Jha, G., Gope, N. & Singh, S. (2006). *Mater. Charact.* **57**, 127–135.

Timokhina, I. B., Hodgson, P. D. & Pereloma, E. V. (2004). *Metall. Mater. Trans. A*, **35**, 2331–2341.

Tjahjanto, D., Turteltaub, S., Suiker, A. & van der Zwaag, S. (2008). *Philos. Mag.* **88**, 3369–3387.

Tomota, Y., Tokuda, H., Adachi, Y., Wakita, M., Minakawa, N., Moriai, A. & Morii, Y. (2004). *Acta Mater.* **52**, 5737–5745.

Zaefferer, S., Ohlert, J. & Bleck, W. (2004). *Acta Mater.* **52**, 2765–2778.